



HAL
open science

Analysis of deformation mechanisms in metal extrusion of 17-4 PH stainless steel: influence of layer thickness and contour number

J. Marae Djouda, M. Ali Bouaziz, François Hild

► **To cite this version:**

J. Marae Djouda, M. Ali Bouaziz, François Hild. Analysis of deformation mechanisms in metal extrusion of 17-4 PH stainless steel: influence of layer thickness and contour number. *Experimental Mechanics*, 2025, 65, pp.467-480. <10.1007/s11340-024-01138-x>. <hal-04913244>

HAL Id: hal-04913244

<https://hal.science/hal-04913244v1>

Submitted on 27 Jan 2025

HAL is a multi-disciplinary open access archive for the deposit and dissemination of scientific research documents, whether they are published or not. The documents may come from teaching and research institutions in France or abroad, or from public or private research centers.

L'archive ouverte pluridisciplinaire **HAL**, est destinée au dépôt et à la diffusion de documents scientifiques de niveau recherche, publiés ou non, émanant des établissements d'enseignement et de recherche français ou étrangers, des laboratoires publics ou privés.



HAL Authorization

Analysis of Deformation Mechanisms in Metal Extrusion of 17-4 PH Stainless Steel: Influence of Layer Thickness and Contour Number

Joseph MARAE DJOUDA^{a,b*}, Mohamed Ali BOUAZIZ^{a,c}, François HILD^b

^a*EPF-Engineering school, 4 avenue du Président Wilson, Cachan, France*

^b*Université Paris-Saclay, CentraleSupélec, ENS Paris-Saclay, CNRSLMPS - Laboratoire de Mécanique Paris-Saclay, Gif-sur-Yvette, France*

^c*Now at CEA, Service d'Étude Des Matériaux Irradiés, Université Paris-Saclay, Gif-Sur-Yvette, France*

*Corresponding author: Joseph MARAE DJOUDA, joseph.marae_djouda@ens-paris-saclay.fr

Abstract:

Background. Metal extrusion additive manufacturing (MEAM) is a cost-effective method for fabricating parts. Understanding the impact of processing parameters and their interactions on mechanical properties remains challenging.

Objective. This study aims to investigate the relationship between layer thickness, number of contours and the deformation mechanisms of 17-4 PH stainless steel parts produced through Atomic Diffusion Additive Manufacturing (ADAM).

Methods. Notched samples were fabricated with two different layer thicknesses (50 μm and 125 μm) and two contour configurations (2 and 4 contours). In-situ tensile tests combined with digital image correlation (DIC) were performed to investigate strain fields.

Results. The results indicate that the layer thickness significantly influences crack propagation, while also interacting with the number of contours. All samples achieved similar notch opening displacements (NOD) at failure. Differences in layer thickness and contour configurations led to distinct deformation mechanisms.

Conclusions. Variations in layer thickness and number of contours affected the deformation mechanisms and crack propagation in parts manufactured by MEAM, underscoring the importance of optimizing these parameters to enhance the mechanical performance.

Keywords: Additive manufacturing; Digital Image Correlation (DIC); Notch opening displacement; Printing parameters; Strain fields

Introduction

Additive manufacturing (AM) techniques enable for the fabrication of parts through a layer-by-layer deposition process, offering advantages such as complex geometry production, reduced lead time, and minimized material waste [1,2]. In recent years, AM has become increasingly robust, allowing for the fabrication of highly reliable components used in aerospace and medical applications [3–5]. Among these techniques, fused deposition modeling (FDM), originally developed for polymers, has been adapted for metal extrusion and presents a cost-effective alternative to powder-based AM processes that rely on high-energy sources such as laser or electron beams [6,7].

Metal extrusion AM processes, including Atomic Diffusion Additive Manufacturing (ADAM) developed by Markforged, use highly-filled polymers with metal particles that are extruded layer by layer to form the desired shape. After extrusion, the polymer binder is removed, and the parts are sintered to achieve dense metallic components [8,9]. Unlike beam-based techniques, where the microstructure forms layer by layer through melting and solidification, the microstructure in metal extrusion AM is formed during sintering, leading to distinct mechanical properties.

While much research has focused on process parameters for polymers in FDM, such as layer thickness, raster angle, and infill density [10–15], less is known about the mechanical behavior of metallic parts produced by extrusion-based AM. The layer thickness, in particular, plays a key role in determining the mechanical properties of printed parts, but few studies have explored its specific influence on metals [16][17]. Moreover, the interaction between layer thickness and other parameters, such as the number of contours, remains poorly understood. The number of contours, which defines the thickness of the outer walls of the printed parts, may influence crack propagation, stress distributions, and overall structural integrity.

In this study, the effect of deposited layer thickness on the deformation mechanisms of 17-4 PH stainless steel fabricated via ADAM is investigated. Two different layer thicknesses (50 μm and 125 μm) are analyzed using in-situ tensile tests coupled with Digital Image Correlation (DIC) to determine strain fields. In addition to the layer thickness itself, the interactions between the number of contours (2 and 4) and the layer thickness are examined to investigate their influence on the fracture behavior. While the primary focus of this study is on the layer thickness, the indirect effects of contouring and infill strategies are also discussed, highlighting the importance of a comprehensive approach to process parameters optimization.

The knowledge gained from this study provides a basis for future research on the combined effects of various parameters in metal extrusion additive manufacturing.

Experiments

Details on the sample fabrication are provided along with the induced microstructure and the in-situ tensile test procedure.

Sample fabrication

Single edge notched tension specimens were used in the present study. They are referred to as “mini-SENT” because of their small dimensions. These specimens are well adapted for in-situ tensile tests on micromachines under optical microscopes or scanning electron microscopes (SEMs). The mini-SENT specimens were fully additively manufactured (including the notch) with dimensions shown in Figure 1(a). The notch dimension met the ASTM E1820 [18] standard recommendations (i.e., specimen width and initial notch depth). They were fabricated by adding molten layers of 17-4 PH filaments using a Markforged machine. The material used in the process was a resin-based filament loaded with the metal powder. The printer unwinds the material spool, heats it up to the resin melting temperature with an extrusion head, and then deposits it as successive layers according to the 3D CAD file. The samples were printed as a solid part, in a flat $\pm 45^\circ$ orientation and different wall contours (Figure 1(b)).

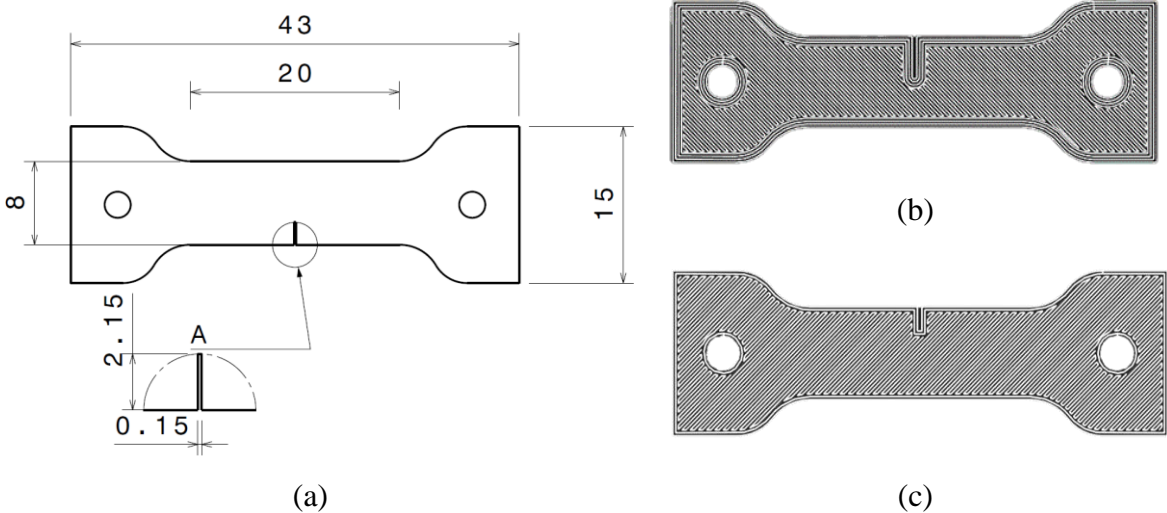


Figure 1: (a) Sample dimensions in mm (thickness =4 mm). (b) One-layer nozzle path when printing samples 125-1, 125-2 and 50-1. (c) Corresponding path for samples 50-2 and 50-3

Samples with two different layer heights, namely, 50 μm and 125 μm were 3D printed with the Metal X machine. The printed green parts were submitted to debinding and sintering processes [19]. The green parts were dipped into Opteon SF-79 solvent of a heated washer for at least 12 h to remove the binding polymer [20]. The parts were air-dried in the bin of the washer for at least 4 h based on Markforged recommendations. After this step, the samples were sintered in a furnace with a controlled environment (i.e., gaz containing 97.3 vol% of Ar and 2.7 vol% of H_2) for 27 h. The sintering consisted of three key steps. In the first stage, the temperature was increased to reach the debinding temperature at which the polymer binder sublimated. Then, the temperature was increased up to 1300°C. Material diffusion took place and the part became dense. Last, the furnace was gradually cooled down until the parts could be safely removed. The parameters used for manufacturing the different specimens are detailed in Table 1. In the following, the layer thickness refers to the layer height.

*Table 1: Printing parameters and specimen designation.
The specimen thickness was measured after mechanical polishing*

Deposited layer thickness (μm)	wall contour number	notch depth (mm)	Specimen thickness (mm)	specimen designation
125	4	3.6	1.44	125-1
	4	3.6	1.47	125-2
50	4	3.6	1.5	50-1
	2	2.15	1.44	50-2
	2	2.15	1.39	50-3

In order to investigate the microstructures generated by the fabrication process and the effect of layer thickness, SEM images and electron backscattered diffraction (EBSD) maps were acquired (Figure 2). Prior to that step, the samples were mechanically polished. 400/600/1200/2400/4000 grit papers were successively used for about 3 min for each step. Polishing cloths with diamond suspensions of 3 μm and 1 μm in diameter were successively used in order to ensure a smooth surface. After polishing, an electrochemical procedure with an oxalic acid bath (10 g of oxalic acid dissolved in 100 ml of demineralized water) was used. The samples were soaked in this solution for 10 s to reveal the surface microstructure.

Sample microstructure

Figure 2(a-b) shows SEM images evidencing the microstructures obtained for 50 μm and 125 μm layer thicknesses. The microstructures are similar for both layer thicknesses. They are composed of grains with an average diameter ranging from 30 μm to 70 μm and contained martensite laths. In addition, defects were also revealed by the combined effects of mechanical polishing and chemical etching, which induced holes (Figure 2(a-b)). The observed microstructure is rather similar to 17-4 PH ones obtained by other AM metallic fabrication techniques. For example, the 17-4 PH microstructure obtained by selective laser melting was characterized as complex directional or columnar lath structures parallel to the build direction [21][22]. In the microstructures obtained herein, the defect population was mainly composed of precipitates.

The martensite laths are more visible in the image quality (IQ) maps associated with Electron backscattered diffraction (EBSD), see Figure 2(c-d). The globular black zones (indicated with red arrows) visible in the IQ maps correspond to precipitates. The presence of globular defects corresponds to copper-rich precipitates [23,24] for 17-4 PH obtained from laser powder bed AM. However, the size and density of globular inclusions observed herein are larger than those typically seen in laser powder bed fusion. Similar pores have been reported for extruded 17-4 PH stainless steel, the black spherical or elliptical particles like those observed herein were identified as SiO_2 particles [23]. The smaller white particles are NbC precipitates. These inclusions result from residual polymers not fully removed during debinding and then transformed during sintering. They may also originate from the powder preparation process. The inverse pole figures (IPF) highlight the typical martensitic microstructure of 17-4 PH made of laths (Figure 2(e-f) [21,25]. In the IPF of the sample fabricated with a layer thickness of 50 μm , the density of unsolved pixels is important, and martensitic laths are thinner. Conversely, the quality in the other sample is better and the IPF shows martensite laths that are packed in the grains.

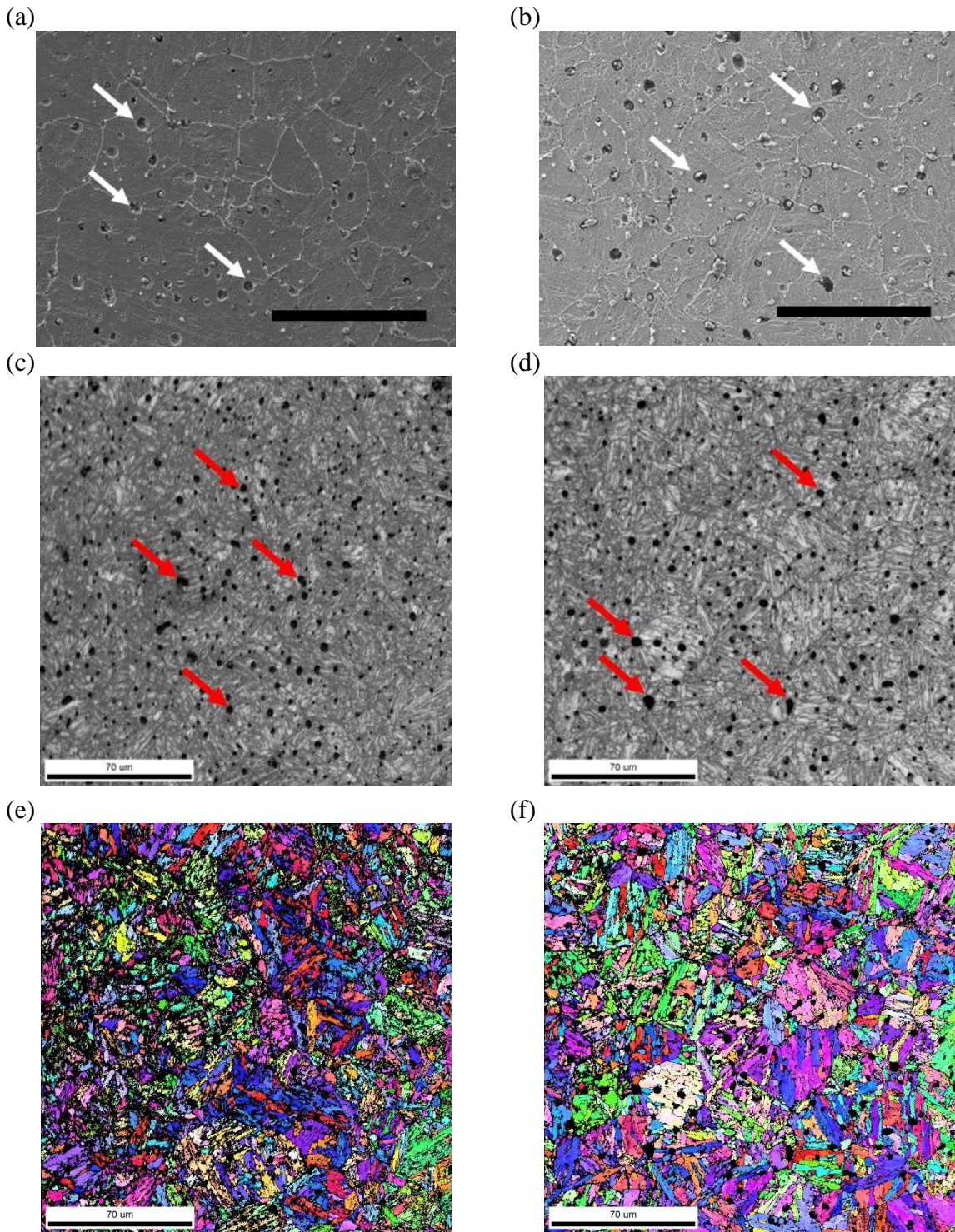
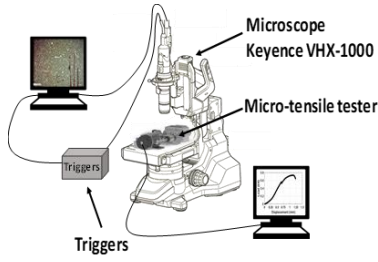


Figure 2: Microstructures of the samples as a function of the thickness of deposited layers, (a) 50 μm and (b) 125 μm , respectively. The image quality maps of microstructures fabricated with 50 μm and 125 μm thick layers are shown in sub-figures (c) and (d). The corresponding inverse pole figures are displayed in sub-figures (e) and (f).

In-situ tensile tests

The samples were mechanically polished on both sides. The thickness was reduced from 4 mm to 1.5 mm (the final thickness for each sample is reported in Table 1) in order to conduct the tests until failure with the capacity of the load cell. One side of the samples was mirror polished allowing the surfaces to be patterned for DIC purposes. White speckles with micrometric dimensions were deposited using an airbrush [26]. The experimental setup consisted of a numerical Keyence VHX-1000 microscope for surface observations, a tensile micromachine and a triggering system (Figure 3(a)). The latter allowed images to be recorded at specific rates when the specimen was continuously loaded, and each image to be related to the corresponding applied force. The crosshead velocity varied between $0.5 \mu\text{m} / \text{s}$ and $1.9 \mu\text{m} / \text{s}$. The global strain rate (i.e., related to the gauge length of the sample) ranged from 2.6×10^{-5} and 10^{-4} s^{-1} (Figure 2(b)).

Regularized DIC was used to measure displacement fields in all the experiments reported hereafter. These raw data were used in two ways. On the one hand, the notch opening displacement (NOD) was assessed to quantify crack opening during the tensile tests. On the other hand, Green Lagrange strain fields were computed by exact derivation of the shape functions of the mesh made of 3-noded triangular (T3) elements. Regularization consists in penalizing the DIC cost function with the equilibrium gap cost function [27]. In the present case, incremental regularization was performed to account for the fact inelasticity occurred [28].



(a)

Microscope	Keyence VHX-1000				
Definition	54 Megapixel 3CCD				
Lens	VH-Z100R (100× to 1000×)				
Image acquisition rate	1 fps				
Load cell	5 kN				
Crosshead velocity ($\mu\text{m/s}$)	125-1	125-2	50-1	50-2	50-3
	1.9	1.1	1.8	0.5	0.5
Field of view	$3.05 \times 2.28 \text{ mm}^2$				
Image scale	$2.1 \mu\text{m} / \text{px}$				
Dynamic range	8 bits				

(b)

Figure 3: (a) Experimental setup used for in situ tensile tests. (b) Experimental parameters for each test.

Notch opening displacement (NOD) analysis

The notch opening displacement (NOD) was measured by choosing two zones of interest (ZOIs) around the notch in order to evaluate the opening displacement. Figure 4(a) illustrates the ZOIs chosen for NOD measurements of specimen 50-3. Both ZOIs were symmetrically positioned about the notch root with an offset of 50 pixels. The same ZOI positioning relative to the notch root was considered for all studied tests. The NOD was obtained by calculating jumps corresponding to the mean vertical displacement difference between the two zones (Figure 4(a)) [29][30]. The DIC analysis parameters for NOD measurements are gathered in Table 2.

Table 2. DIC analysis parameters for NOD measurements

DIC software	Correli 3.0 [31]
ZOI size	$2 \times (100 \times 100)$ pixels (Figure 5(a))
Element size	$\ell_{FE} = 9 \text{ px}$
Mechanical regularization length	50 px
Matching criterion	regularized sum of squared differences
NOD noise-floor (nm)	3

The NOD variations characterize the global deformation around notches at the macroscopic scale [29] (Figure 4(b)). Clear differences are observed as a function of layer thickness. Samples 50-2 and 50-3, which were tested with the same experimental parameters, reached very close NOD levels at failure (Table 3). The difference between these two tests and sample 50-1 is due to the fact that the initial notch length, the number of wall contours, and crosshead velocity were not the same (Table 1). Conversely, the geometry of sample 50-1 was very close to that of samples 125-1 and 125-2. It led to a similar evolution in terms of NODs.

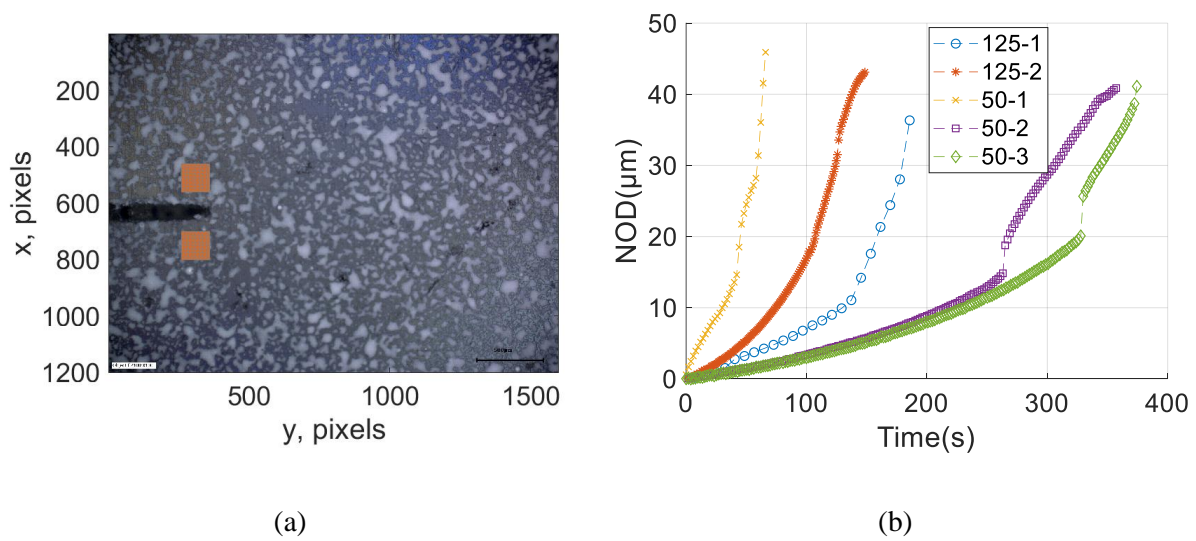


Figure 4: (a) Relative position of ZOIs where the displacement from both sides of the notch is calculated to assess NODs (sample 50-3). (b) NOD histories in the five tensile tests.

It is worth noting that sudden changes in crack opening displacement, visible around 20 μm of NOD, occurred for all samples with a 50 μm layer thickness. This observation evidences the fact that similar mechanical evolutions were obtained with samples fabricated with the same processing parameters (except for geometrical parameters) due to the generated microstructure. Thus, the process is deemed reproducible. The difference in critical NODs (i.e., ultimate NOD level prior to failure) are not significant (i.e., less than 5 μm , see Table 3). The failure behavior seems not influenced especially by the deposited layer thickness.

The applied crosshead velocities were different for specimens 125-1 and 125-2. However, the same features were observed for these two specimens in comparison to the other three. The influence of the applied velocity during the tensile test is deemed minimal for the

range investigated in this study. These results confirm the reproducibility of the fabrication process and highlight the fact the material did not undergo viscoplasticity.

Table 3: Ultimate NODs for all tested samples

Specimen designation	NOD_c (μm)
125-1	36.3
125-2	43.1
50-1	45.9
50-2	40.9
50-3	41.1
Mean	41.5
Standard deviation	3.5

Analyses of optical images

An analysis of optical images acquired during the in-situ tensile tests gives access to a first set of observations. Figure 5 shows the mean longitudinal strain ϵ_{yy} as a function of the NOD, and images at specific NOD values for specimen 50-3. The mean strain was obtained from strains fields measured via DIC. This analysis allows the initiation and propagation of the crack at the specimen surface to be qualitatively understood.

The comparison in crack growth from the optical images of the specimen is then possible. For the image corresponding to $NOD = 19.3 \mu\text{m}$, crack propagation is effective and the crack path is oriented downward. The sudden crack propagation event for NOD levels ranging from $19.3 \mu\text{m}$ to $24.8 \mu\text{m}$ resulted in subsequent upward propagation. The relative angle between the cracks is close to 90° , which corresponds to the filament angle of two adjacent layers in the $\pm 45^\circ$ infill configuration. Then, the directions of crack propagation are related to the layer deposition architecture. The important change in NOD levels between these two images is also noticed in the curve of mean strain as a function of NOD. The crack propagated continuously until sample failure for $NOD_c = 41.1 \mu\text{m}$. On the last image recorded few moments before specimen failure, the visible crack propagation distance was estimated to

be about 1 mm. The green circle depicts the damage marks at the junction of crossed filaments in adjacent layers.

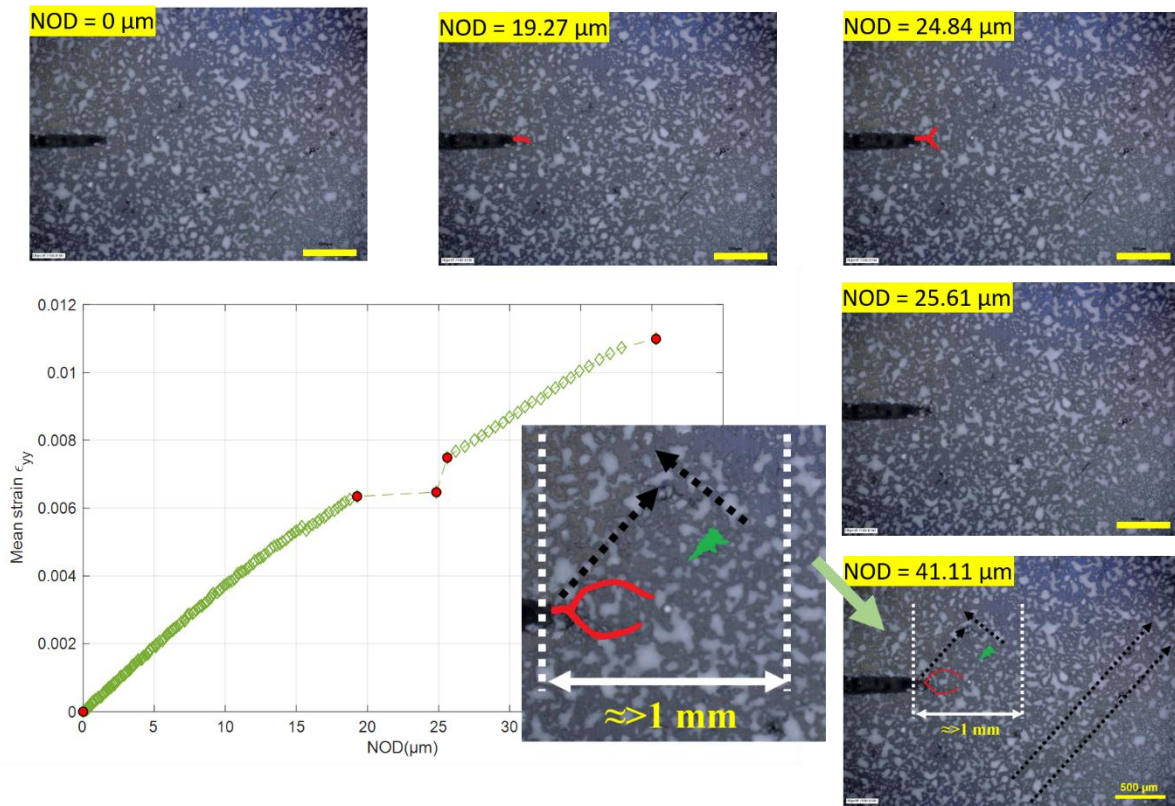


Figure 5: Qualitative analysis of crack propagation during the in-situ tensile test on sample 50-3. The position of these images is indicated on the mean strain vs. NOD curve by red points and NOD corresponding value is superimposed on the images. The yellow dashed lines depict the crack propagation path through the contours. The scale bar represents 500 μm .

Kinematic field analysis

The DIC measurements allows for quantitative analyses of strain fields of the sample surfaces and then for an understanding of the deformation mechanisms.

Strain fields analysis

For more in-depth analyses, the strain fields at the specimen surfaces are reported. Table 4 gathers the parameters of this new set of DIC runs. To evaluate the measurement uncertainties, preliminary analyses were conducted on 10 images prior to the tests of samples 50-2 and 50-3. The standard uncertainties were estimated by calculating the noise-floor levels for longitudinal displacement and strain fields. For both tests, the standard uncertainties were about 0.02 μm for displacements and 10^{-4} for longitudinal strains.

Table 4. DIC analysis parameters to assess strain fields

DIC software	Correli 3.0 [31]
ROI size	800 × 1000 pixels
Element size	$\ell_{FE} = 4$ pixels
Mechanical regularization length [32]	30 pixels
Matching criterion	regularized sum of squared differences
Strain calculation	exact derivation of shape functions
Strain window	element

Figure 6(a) displays the mean longitudinal strain ε_{yy} histories for the five tests. Specimens 50-2 and 50-3 led to similar changes in deformations because of the fact that their fabrication (Table 1) and testing conditions (Figure 2(b)) were close. The mean strain of specimen 50-1 increases considerably at the end of the test. Samples 50-2 and 50-3 present similar mean strain histories, which are attributed to their identical printing parameters (in addition to the layer thickness). Samples 50-1, 125-1 and 125-2 each show distinct strain changes. It is worth noting that even samples 125-1 and 125-2 with similar printing parameters have different mean strain histories. Furthermore, sample 50-1 displays a unique strain evolution compared to the other samples with the same layer thickness, which is likely due to its four contours, while the other two samples only had two contours.

Figure 6(b) shows the corresponding NOD vs. means strain ε_{yy} changes. Apart from samples 50-2 and 50-3 which had similar trend, the other ones had specific histories. The responses of specimens with 50 μm layer thickness lie between those of 125 μm samples. This result shows that the layer thickness had a limited influence on the macroscopic NOD vs. ε_{yy} response in line with the fact that the critical values of NODs were very close (Table 3).

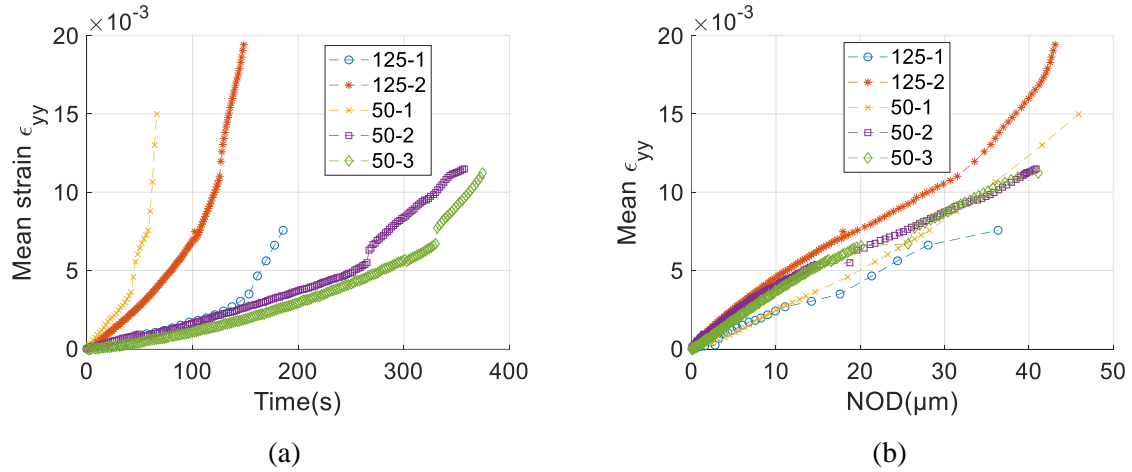


Figure 6: (a) Temporal changes of mean strains extracted from FE-DIC analyses at the surface of the five specimens. (b) Mean strains as functions of NODs.

The strain maps corresponding to the images shown in Figure 5 are presented in Figure 7. For the image corresponding to $\text{NOD} = 16.5 \mu\text{m}$, the highest strain concentration is located at the root of the notch. Strained bands emanate from the notch root and are oriented at $\pm 45^\circ$. The strain concentration is more significant in the band oriented downward. This observation may explain why this downward band was first visible in the optical images, while the upward band was not in the first two images shown in Figure 5. These bands correspond to the junction of two filaments deposited in the same layer. Then, the crack seeks for weaker zones to propagate, which, in that case, correspond to the inter-filament junctions. By increasing the applied load, the strain concentrations increased in bands aligned along the $\pm 45^\circ$ directions. This observation indicates that the sample welding zones between adjacent filaments in layers are weak points.

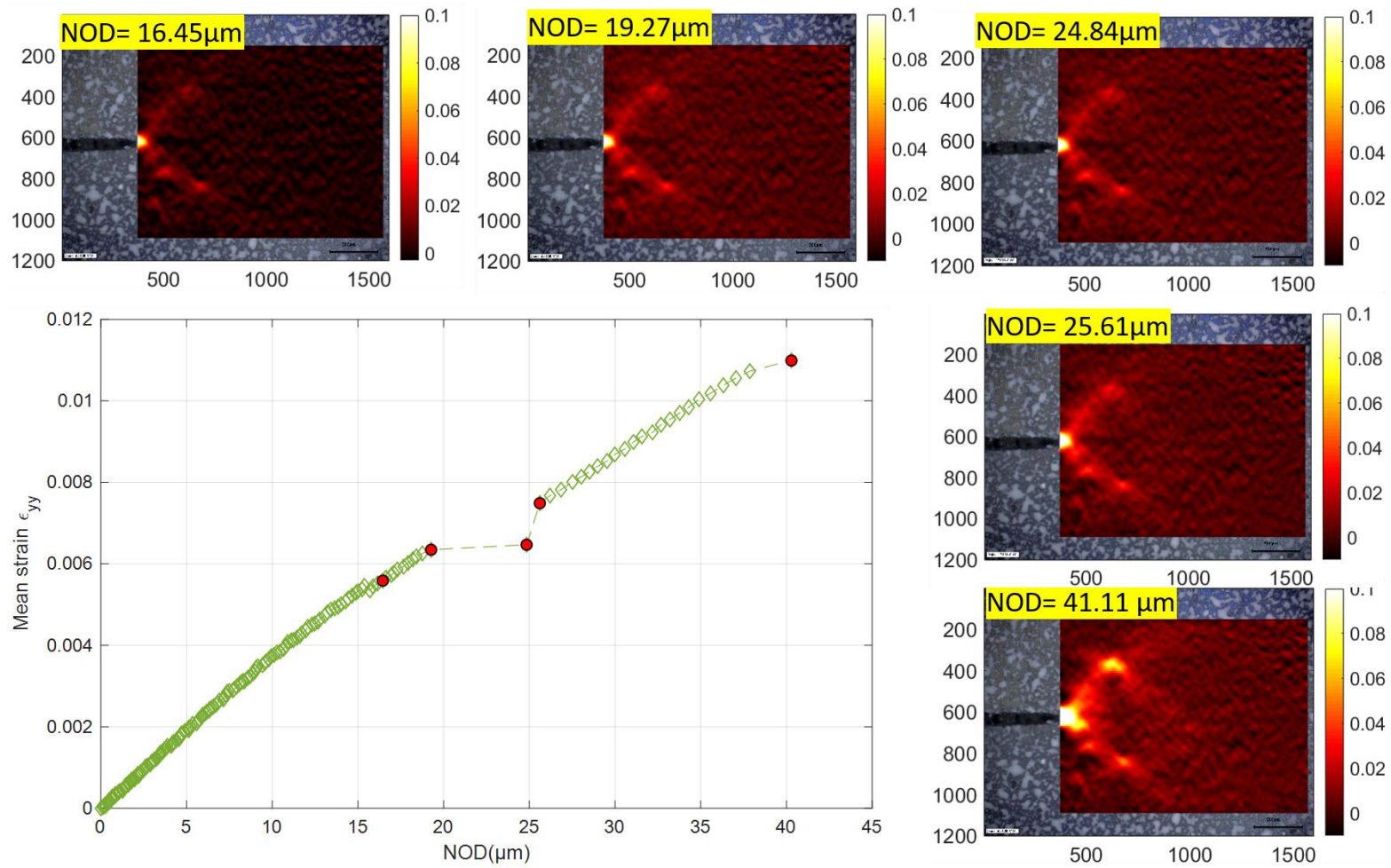


Figure 7: Analysis of crack propagation during the in-situ tensile test on sample 50-3. The red points in the curve of NOD vs. mean strain ϵ_{yy} indicate the levels at which the images have been recorded. A sudden propagation in NOD is observed between the images corresponding to NOD = 19.3 μm and 24.8 μm .

Crack propagation was still limited before the image corresponding to $NOD = 25.6 \mu\text{m}$. At this level, the strain concentrations in the $\pm 45^\circ$ bands were similar. The strain maps reveal that the two strained bands were formed earlier ($NOD = 16.45 \mu\text{m}$). This result confirms the interest of using DIC at a local scale. As the applied load further increased, crack propagation and strain concentrations in bands increased, the zones corresponding to junctions of filaments of two adjacent layers experienced strain concentrations ($NOD = 41.1 \mu\text{m}$). This observation means that bands propagated from one side and arrived at the other end of the filaments. The strain bands originated from the notch seem to be stopped after the crossed filaments. The crossed filaments in adjacent layers behave like strain barrier. In the present case, the junction at the upward band experienced the highest strain concentrations. The sample fracture may arise from this upward band.

Apart from the strain maps corresponding to specimen 50-3, the other strain maps are now commented at the beginning of each test ($NOD = 5 \mu\text{m}$), in the plastic domain ($NOD = 20 \mu\text{m}$) and just before specimen failure. Figure 8 presents the corresponding strain maps for the three specimens fabricated with a $50 \mu\text{m}$ layer thickness. The strain distributions and changes for specimen 50-1 are different from those of specimens 50-2 and 50-3. In specimen 50-1, the crack has the highest propagation compared to the other two specimens. After considerable straight propagation, the crack forked and propagated further before final fracture. For samples 50-2 and 50-3, straight crack propagation remained limited. However, for these specimens, strain concentrations appeared on both sides of the crack and were symmetric with respect to the notch root. Moreover, $\pm 45^\circ$ bands formed at high strain levels and followed the way the specimens were fabricated. Then, the crack propagation length was influenced by the number of contours used for the notch. The infill strategy is also visible in the deformation mechanisms and sample failure.

The main difference between sample 50-1 and the others with $50 \mu\text{m}$ layer thickness was the number of wall contours (Table 1); it had 4 contours, while the others had 2. These wall contours were used for the notch fabrication and played an important role in terms of crack propagation and deformation mechanism. Specimen 50-1, with the highest number of walls, experienced more stable crack propagation. For the others, stable crack propagation was more limited. Interestingly, even though the crack length was different, the critical NODs were very close (Table 3).

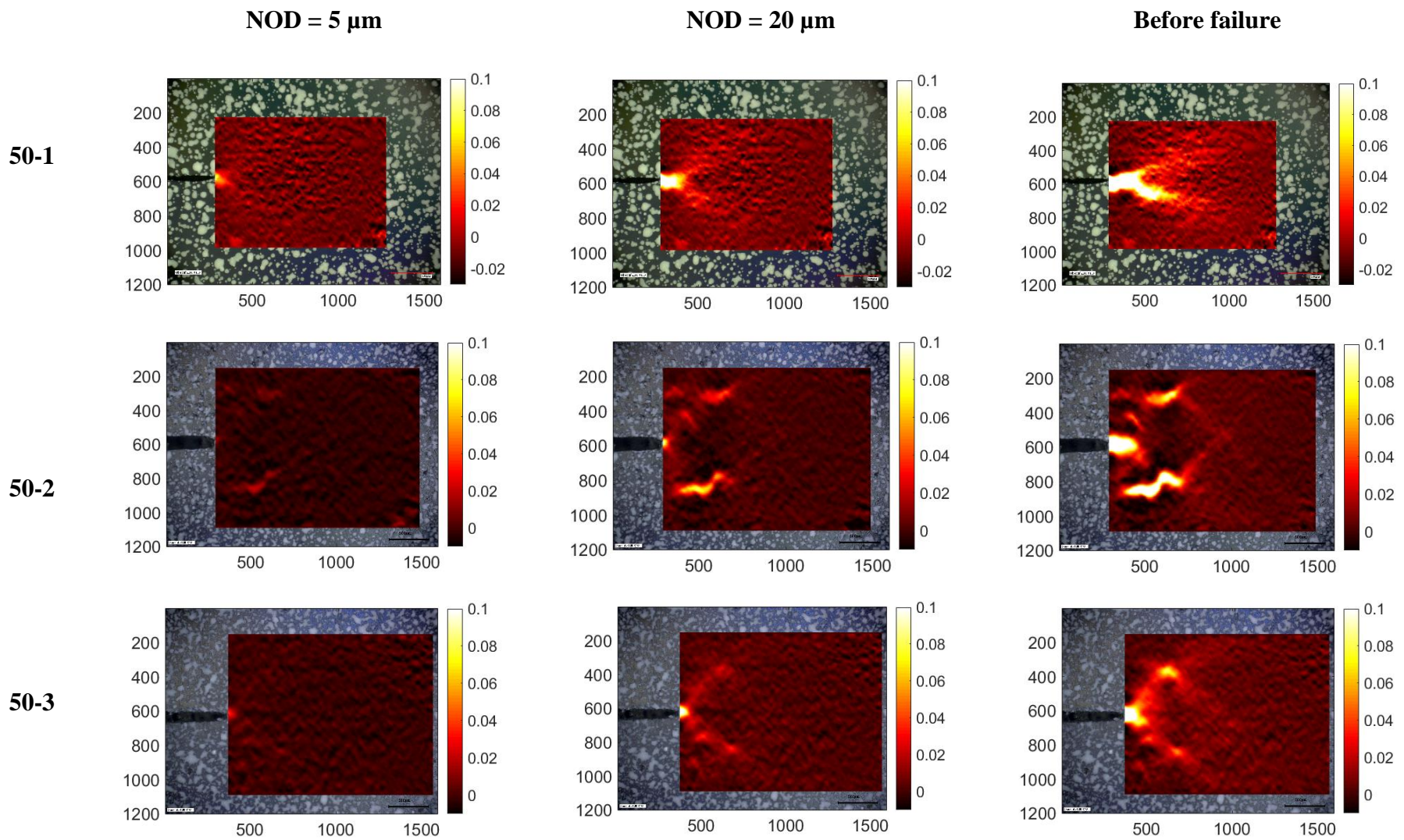


Figure 8: Strain maps for specimens with 50 μm layer thickness at different NOD levels.

For the samples with 125 μm thick layers, the strain maps are reported in Figure 9. Crack propagation was completely different from what was observed in the specimens with smaller layer thicknesses (Figure 8). Crack propagation remained very limited. The strains mainly concentrated between wall contours, which are essential since they are helpful to achieve complex geometries. However, their deformation led to strained bands between each individual contour, whose level increased with the applied load. In sample 125-1, the crack propagation length was very small even before failure, and strain concentrations at contour junctions are visible in the upper region of the notch.

In the strain maps of specimen 125-2, the boundaries of wall contours are observed when $\text{NOD} = 5 \mu\text{m}$. The corresponding strain concentrations increased with the applied load. In the strain map corresponding to the image acquired just before sample failure, the last boundary of wall contours experienced the highest strain levels. For this sample, fracture likely initiated at the last boundary of the wall contours and induced the final event. This observation confirms that the wall contours play a key role in the deformation patterns at a local scale according to their number and the thickness of the layers.

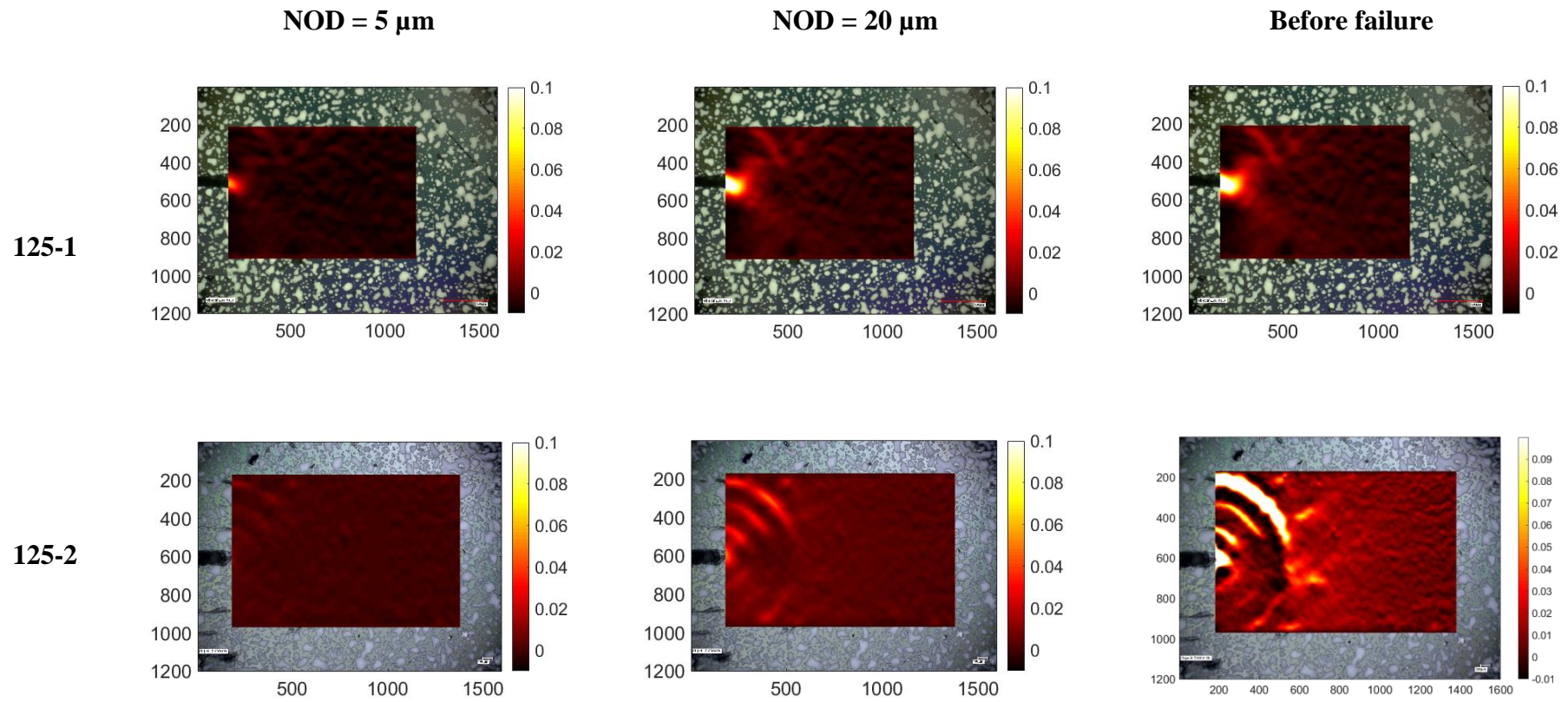


Figure 9: Strain maps for specimens with 125 μm layer thickness for different NOD levels.

Strain rate maps

The strain maps ε_{yy} shown in Figure 8 do not reveal the origin of the gap observed in NOD levels, which is a signature of crack initiation. The only significant feature in the strain fields is an increase of the strain magnitude in the two $\pm 45^\circ$ bands. Besides these limited variations visible on the strain maps in the tensile direction, the corresponding values of NODs showed important variations. In order to further investigate the sudden propagation steps, the strain rate maps are reported for sample 50-3 in Figure 11 when crack initiation occurred. For the loading steps corresponding to NOD = 16.5 μm , 19.3 μm and 24.8 μm , the strains remained very low and concentrated in the immediate vicinity of the notch root (Figure 8). The strain rate maps corresponding to these levels present also strain increment with a small level at the notch root. When the applied load increased, higher concentrations are observed around the notch root as well as the two bands oriented at $\pm 45^\circ$. They are also observed in the strain rate map corresponding to NOD = 25.6 μm . This trend is similar to that seen in the optical image corresponding to NOD = 24.8 μm (Figure 5).

For the strain rate map corresponding to NOD = 26.6 μm , the strain concentration was again localized around the notch root. In the last two maps of Figure 10, the amplitude in strain concentrations was higher than those observed in the earlier strain rate maps (NOD = 16.5 μm , 19.3 μm and 24.8 μm). The sudden propagation step observed in NOD data resulted locally from crack bifurcation and propagation. For NOD = 24.8 μm , the sudden increase in NOD is visible and the strain rate map and macroscopic response (NOD vs. mean strain ε_{yy}) show very low variations. In the next image (NOD = 25.6 μm), the NOD variation is coupled with strain amplification.

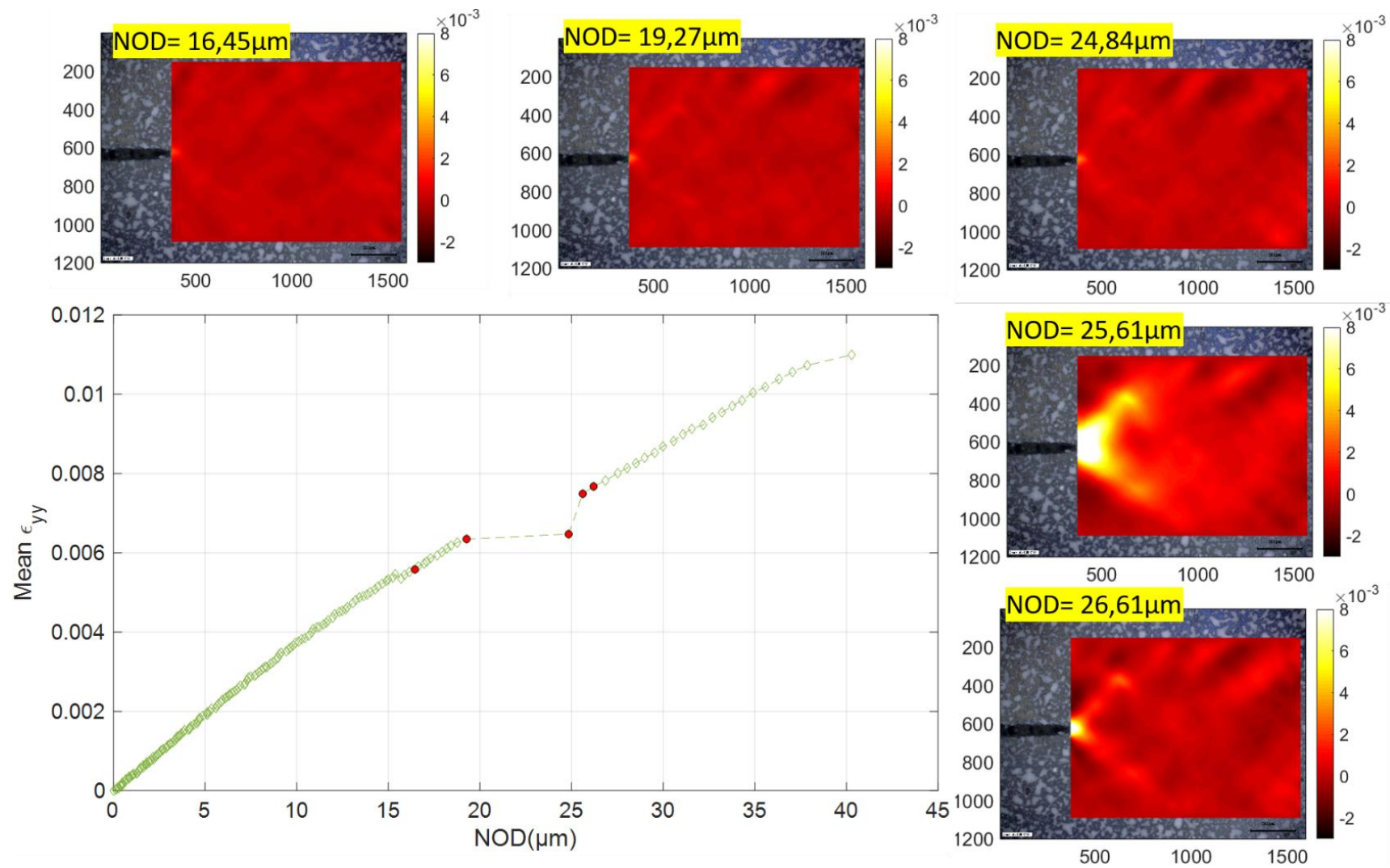


Figure 10: Strain rate (expressed in s^{-1}) maps around the sudden propagation step for sample 50-3.

Fracture analysis

The optical images of specimens after failure are compared with strain maps corresponding to the last recorded images before failure. The fractographies of the samples are also analyzed.

Failure mechanism

The analysis of the fractured samples may further inform on the failure mechanisms. This analysis includes all tested samples (Figure 11) in which optical micrographs of the crack path are compared with the strain maps corresponding to the last image recorded before sample failure.

For specimen 50-1, crack propagation is observed through all four contours. After the first contour, the crack attempted an upward bifurcation that was interrupted. Once, the crack reached the last contour, it bifurcated upward, and sample fracture then occurred. The propagation path was straight. It is worth noting that the strains also accumulated between wall contours. This observation indicates that crack propagation occurred along wall contours. It again demonstrates how important they are in the design of AM structures.

For specimens 50-2 and 50-3, the optical micrographs show that fracture occurred after the two wall contours were broken. However, the strains also accumulated in junctions between the second (last) wall contour and the part of the sample where the layers were successively oriented at $\pm 45^\circ$. These strain concentrations appear as bands and marked the locations where they accumulated. They were symmetric relative to the crack propagation path from the notch root. In the micrograph of specimen 50-2, after the crack traversed the two wall contours, it first propagated along the $+45^\circ$ direction for a few micrometers, and then bifurcated in the -45° direction. This zigzagged path indicates that the crack sought weak zones between layers to propagate. The crack length in these two specimens is correlated to the length of the two wall contours (of approximately 100 μm).

For the specimens with a deposited layer thickness of 50 μm , crack propagation before failure depends on the number of wall contours, namely two (for specimens 50-1 and 50-2) and four (for specimen 50-1). The crack length is thus correlated to the number of wall contours.

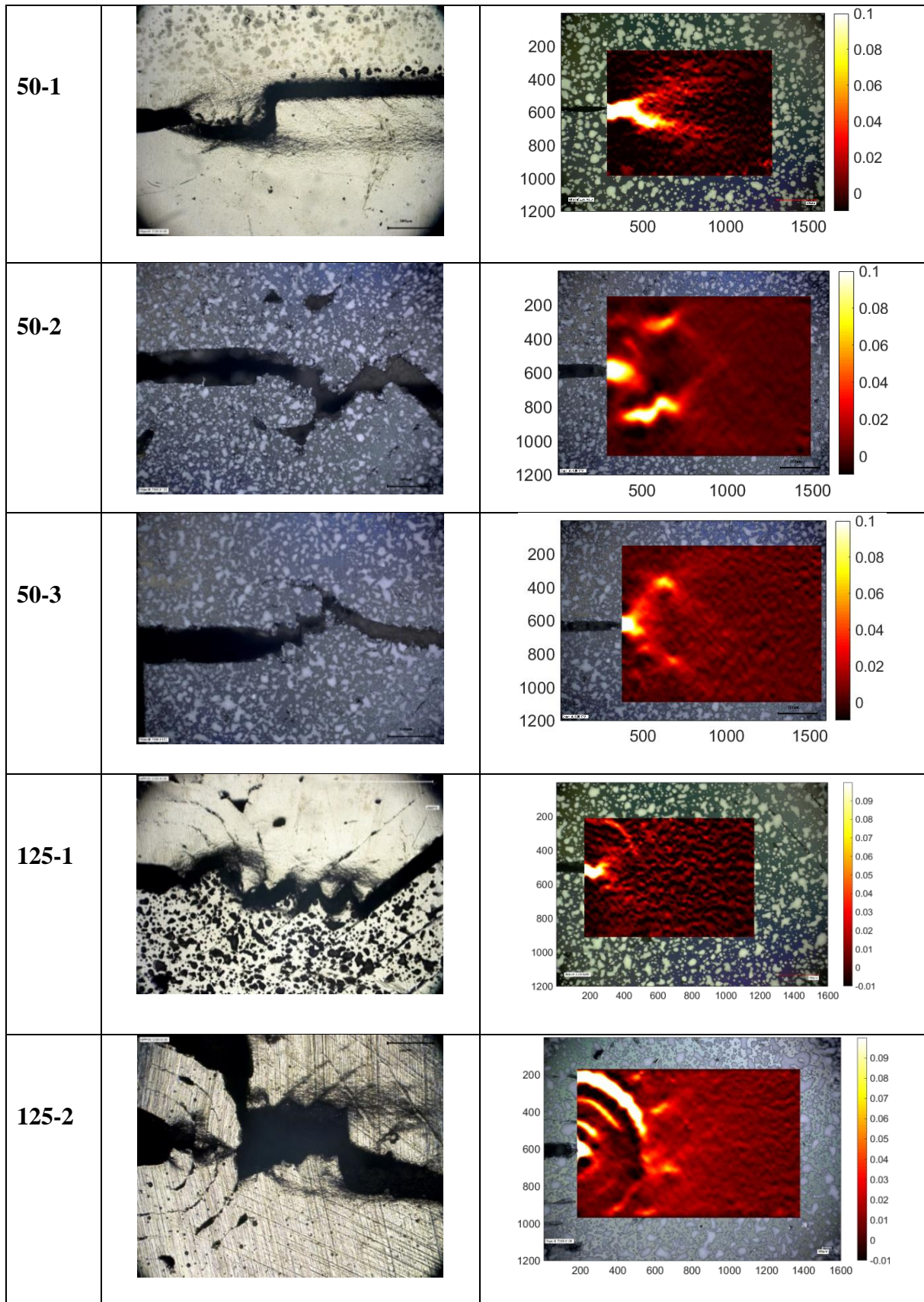


Figure 11: Post-mortem optical micrographs and longitudinal strain maps prior to fracture.

Specimens 125-1 and 125-2 were designed with four wall contours. The corresponding micrographs show considerable deformation at the junctions between the contours. The strain maps show that the strain levels at the contour junctions were not evenly distributed. The junction of the (last) contour with the layers oriented at $\pm 45^\circ$ experienced the highest values. Stable crack propagation was limited in these specimens and was shorter compared to those with 50 μm thick layers.

It is worth remembering that samples 50-1, 125-1 and 125-2 were fabricated with the same parameters except for the layer thickness. It is thus evidenced that with the present manufacturing (ADAM) process, the mesostructure obtained by changing the thickness of deposited layers reacted differently during their deformation. The junctions between 50 μm thick layers were better welded than those with thicker (125 μm) architectures. Despite these differences, the critical NODs were similar. The analysis of strain maps highlights differences in crack propagation, deformation mechanisms and sample failure.

Fractured surfaces

SEM fractographies were performed to obtain more details on the deformation and failure mechanisms (Figure 12). The successive layers deposited during sample fabrication are visible along the specimen width. The crossings of the filaments oriented at $\pm 45^\circ$ during the infill strategy are more discernable in the samples with 125 μm thick layers. The boundaries between adjacent contours (indicated by yellow arrows) and between the last contour and the $\pm 45^\circ$ deposition pattern (red arrows) contained large holes. The largest holes in the last boundary are related to filling challenges due to the circular shape of the notch (Figure 1(b-c)) and the thickness of deposited layers. The smaller the thickness of the deposited layer, the better the infill of complex regions. This observation explains why the porosities in the contour boundaries of samples with 50 μm layers were smaller compared to the other ones.

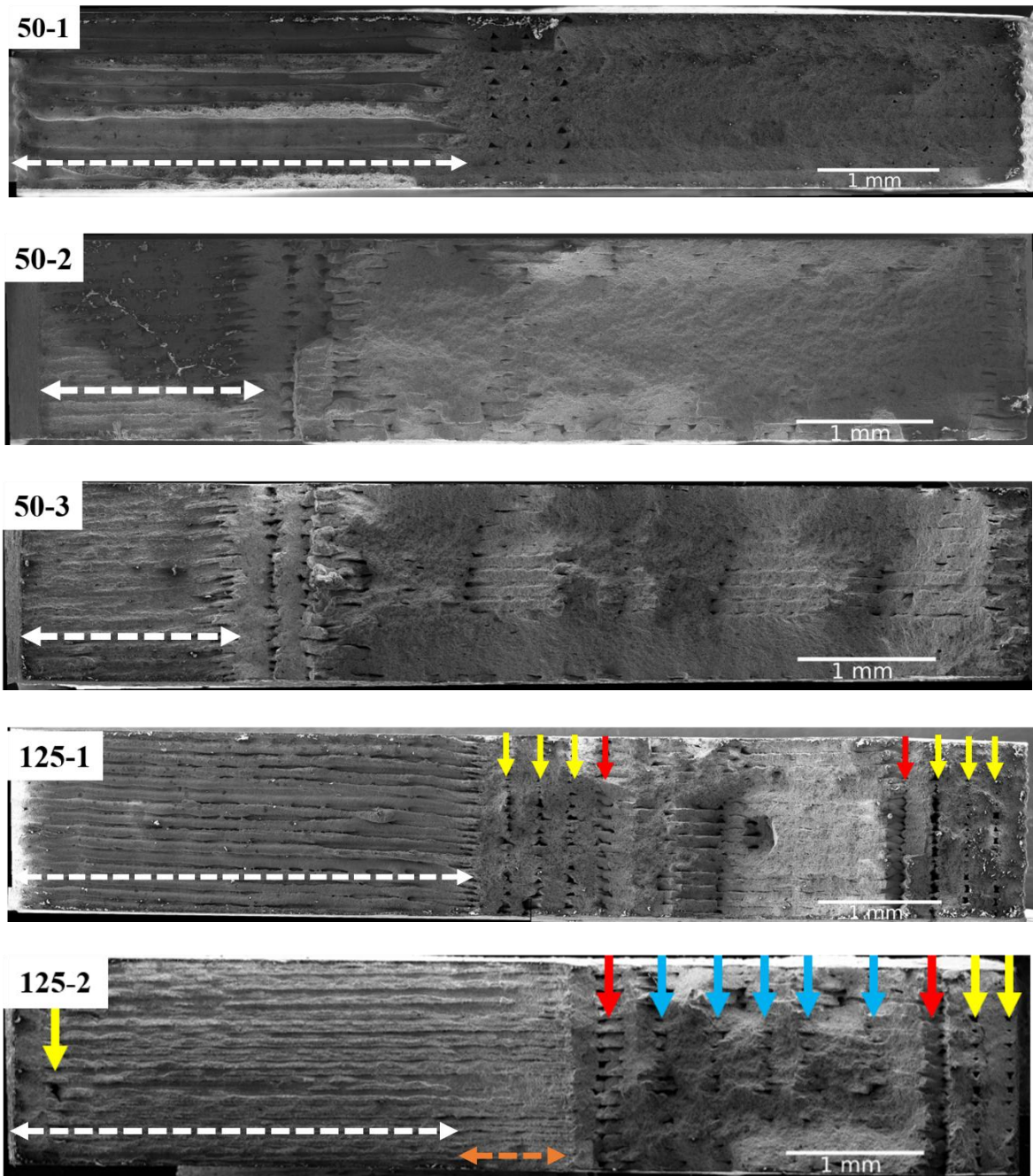


Figure 12: SEM images of the fractured surfaces of the five samples. The white double arrows depict the initial notch length. The orange double arrow on sample 125-2 represents the length over which delamination occurred. The red arrows indicate the boundary between the last contour and the infill. The yellow and blue arrows highlight the contour boundaries and the interlayer crossings, respectively.

The notches of the samples used in this study were additively fabricated. The contours define the external structure of the sample during fabrication. Based on the strain maps, the

strain concentrations at the boundary contours vary depending on the deposited layer thickness. Since notches were made of contours, crack propagation required these contours to be broken; specifically, the first contour must fail before the crack can advance. The challenges associated with breaking these contours, explain the strain concentrations on the boundaries of these contours (Figure 12) especially for samples with 125 μm thick layers. High porosity content at the boundary between the last contour and the $\pm 45^\circ$ deposition led to failure when the crack broke the last contour.

The as-fabricated notch dimensions are reported in Table 1 and geometry in Figure 1(b-c). Samples 50-2 and 50-3 had the same initial notch size. The square edges of the notch led in that case to high strain concentrations on either side of crack propagation. Sample 50-1 and the two samples with 125 μm layers (125-1 and 125-2) had circular contours. The contour shape is highlighted in the corresponding strain maps and optical micrographs (Figure 12). It also appears that the strain concentrations at contour boundaries are enhanced for the samples with 125 μm layer thickness. The boundary of contours of these samples exhibit large holes that weaken them mechanically. The fractography of sample 125-2 presents an initial notch length larger than samples 125-1 and 50-1. This difference is due to the delamination that occurred at the boundary between the last contour and the $\pm 45^\circ$ deposition pattern, which led to failure. This phenomenon is visible on the fractured surface where the breakage of the last longitudinal contour is seen (Figure 12). The final crack propagation step that led to failure started after the last contour (Figure 12). The deformation mechanisms in the vicinity of the notch are dependent on the deposited layer thickness. This feature determines the quality of welding at contour boundaries.

Conclusion

This study analyzed the effect of layer thickness on the deformation mechanisms of 17-4 PH stainless steel samples fabricated using Atomic Diffusion Additive Manufacturing (ADAM). Two different deposited layer thicknesses (50 μm and 125 μm) were tested. It was observed that despite this difference, all samples reached similar notch opening displacement (NOD) levels at failure. The strain maps revealed that the layer thickness interacted with contouring and infill strategies, thereby leading to different deformation mechanisms. Samples with 50 μm layers experienced more stable crack propagation through the contours, while those with 125 μm layers displayed strain accumulations at contour junctions, with limited crack propagation. These differences in fracture behavior highlight the importance of considering

both layer thickness and contour/infill design when optimizing the mechanical performance of parts fabricated by metal extrusion. The fractographic analyses confirmed these findings, showing that the crack length was greater in the 50 μm layer samples, whereas failure in the 125 μm samples was driven by strain accumulations at contour junctions.

Future work needs to investigate the interaction between layer thickness and other processing parameters such as contour and infill strategies, to further improve the mechanical performance and reliability of parts manufactured by MEAM.

Declaration

This work was supported by Region Grand Est (France) under the project NANO-FAB, 18-GE5-027.

Ethical Statement/Conflict of Interest

We have no conflicts of interest to disclose.

References

- [1] I. Gibson, D. Rosen, B. Stucker, *Additive Manufacturing Technologies*, 2014.
<https://doi.org/https://doi.org/10.1007/978-1-4939-2113-3>.
- [2] S.A.M. Tofail, E.P. Koumoulos, A. Bandyopadhyay, S. Bose, L. O'Donoghue, C. Charitidis, *Additive manufacturing: scientific and technological challenges, market uptake and opportunities*, *Mater. Today*. 21 (2018) 22–37.
<https://doi.org/10.1016/j.mattod.2017.07.001>.
- [3] J.H. Martin, B.D. Yahata, J.M. Hundley, J.A. Mayer, T.A. Schaedler, T.M. Pollock, *3D printing of high-strength aluminium alloys*, *Nature*. 549 (2017) 365–369.
<https://doi.org/10.1038/nature23894>.
- [4] T.D. Ngo, A. Kashani, G. Imbalzano, K.T.Q. Nguyen, D. Hui, *Additive manufacturing (3D printing): A review of materials, methods, applications and challenges*, *Compos. Part B Eng.* 143 (2018) 172–196. <https://doi.org/10.1016/j.compositesb.2018.02.012>.
- [5] T. Primo, M. Calabrese, A. Del Prete, A. Anglani, *Additive manufacturing integration with topology optimization methodology for innovative product design*, *Int. J. Adv. Manuf. Technol.* 93 (2017) 467–479. <https://doi.org/10.1007/s00170-017-0112-9>.
- [6] P.A. Hooper, *Melt pool temperature and cooling rates in laser powder bed fusion*, *Addit. Manuf.* 22 (2018) 548–559. <https://doi.org/10.1016/j.addma.2018.05.032>.
- [7] M. Armstrong, H. Mehrabi, N. Naveed, *An overview of modern metal additive manufacturing technology*, *J. Manuf. Process.* 84 (2022) 1001–1029.
<https://doi.org/10.1016/j.jmapro.2022.10.060>.
- [8] G. Wu, N.A. Langrana, R. Sadanji, S. Danforth, *Solid freeform fabrication of metal components using fused deposition of metals*, *Mater. Des.* 23 (2002) 97–105.
[https://doi.org/10.1016/s0261-3069\(01\)00079-6](https://doi.org/10.1016/s0261-3069(01)00079-6).
- [9] I. Campbell, T. Wohlers, *Markforged: Taking a different approach to metal Additive Manufacturing*, *Met. AM.* 3 (2017) 113–115. www.metal-am.com.
- [10] W. Wu, P. Geng, G. Li, D. Zhao, H. Zhang, J. Zhao, *Influence of layer thickness and raster angle on the mechanical properties of 3D-printed PEEK and a comparative*

- mechanical study between PEEK and ABS, *Materials (Basel)*. 8 (2015) 5834–5846.
<https://doi.org/10.3390/ma8095271>.
- [11] S. Terekhina, I. Skorniyakov, T. Tarasova, S. Egorov, Effects of the Infill Density on the Mechanical Properties of Nylon Specimens Made by Filament Fused Fabrication, *Technologies*. 7 (2019) 57. <https://doi.org/10.3390/technologies7030057>.
- [12] M. Lalegani Dezaki, M.K.A. Mohd Ariffin, S. Hatami, An overview of fused deposition modelling (FDM): research, development and process optimisation, *Rapid Prototyp. J.* 27 (2021) 562–582. <https://doi.org/10.1108/RPJ-08-2019-0230>.
- [13] M.M. Hanon, L. Zsidai, Q. Ma, Accuracy investigation of 3D printed PLA with various process parameters and different colors, *Mater. Today Proc.* 42 (2021) 3089–3096.
<https://doi.org/10.1016/j.matpr.2020.12.1246>.
- [14] A. Forés-Garriga, M.A. Pérez, G. Gómez-Gras, G. Reyes-Pozo, Role of infill parameters on the mechanical performance and weight reduction of PEI Ultem processed by FFF, *Mater. Des.* 193 (2020) 108810.
<https://doi.org/10.1016/j.matdes.2020.108810>.
- [15] S.W. Tieuana Tientcheu, J. Marae Djouda, M.A. Bouaziz, E. Lacazedieu, A review on fused deposition modeling materials with analysis of key process parameters influence on mechanical properties, *Int. J. Adv. Manuf. Technol.* 130 (2023) 2119–2158.
<https://doi.org/10.1007/s00170-023-12823-x>.
- [16] S. Terry, I. Fidan, K. Tantawi, Preliminary investigation into metal-material extrusion, *Prog. Addit. Manuf.* 6 (2021) 133–141. <https://doi.org/10.1007/s40964-020-00151-5>.
- [17] M. Drummond, A. Eltaggaz, I. Deiab, 3D Printing of high melting iron alloys using metal-fused deposition modeling: a comprehensive review, *Int. J. Adv. Manuf. Technol.* 129 (2023) 1–22. <https://doi.org/10.1007/s00170-023-12189-0>.
- [18] ASTM-E1820–11, Standard test method for measurement of fracture toughness, in: *ASTM, Annu. B. Stand.* 3, 2011.
- [19] Z. Lotfizarei, A. Mostafapour, A. Barari, A. Jalili, A.E. Patterson, Overview of debinding methods for parts manufactured using powder material extrusion, *Addit.*

- Manuf. 61 (2023) 103335. <https://doi.org/10.1016/j.addma.2022.103335>.
- [20] M. Naim, M. Chemkhi, J. Kauffmann, A. Alhussein, Taguchi DoE analysis and characterization of 17-4 PH stainless steel parts produced by material extrusion (MEX) process, *Adv. Ind. Manuf. Eng.* 8 (2024) 100138. <https://doi.org/10.1016/j.aime.2024.100138>.
- [21] L.E. Murr, E. Martinez, J. Hernandez, S. Collins, K.N. Amato, S.M. Gaytan, P.W. Shindo, Microstructures and properties of 17-4 PH stainless steel fabricated by selective laser melting, *J. Mater. Res. Technol.* 1 (2012) 167–177. [https://doi.org/10.1016/S2238-7854\(12\)70029-7](https://doi.org/10.1016/S2238-7854(12)70029-7).
- [22] H.R. Lashgari, C. Kong, E. Adabifiroozjaei, S. Li, Microstructure, post thermal treatment response, and tribological properties of 3D printed 17-4 PH stainless steel, *Wear.* 456–457 (2020). <https://doi.org/10.1016/j.wear.2020.203367>.
- [23] Y.H. Cho, S.Y. Park, J.Y. Kim, K.A. Lee, 17-4PH stainless steel with excellent strength–elongation combination developed via material extrusion additive manufacturing, *J. Mater. Res. Technol.* 24 (2023) 3284–3299. <https://doi.org/10.1016/j.jmrt.2023.03.228>.
- [24] R. Schroeder, G. Hammes, C. Binder, A.N. Klein, Plasma Debinding and Sintering of Metal Injection Moulded 17-4PH stainless steel, *Mater. Res.* 14 (2011) 564–568. <https://doi.org/10.1590/S1516-14392011005000082>.
- [25] Y. Sun, R.J. Hebert, M. Aindow, Effect of heat treatments on microstructural evolution of additively manufactured and wrought 17-4PH stainless steel, *Mater. Des.* 156 (2018) 429–440. <https://doi.org/10.1016/j.matdes.2018.07.015>.
- [26] J. Marae Djouda, D. Gallitelli, M. Zouaoui, A. Makke, J. Gardan, N. Recho, J. Crépin, Local scale fracture characterization of an advanced structured material manufactured by fused deposition modeling in 3D printing, *Frat. Ed Integrita Strutt.* 14 (2020) 534–540. <https://doi.org/10.3221/IGF-ESIS.51.40>.
- [27] D. Claire, F. Hild, S. Roux, A finite element formulation to identify damage fields : the equilibrium gap method, *Int. J. Numer. Methods Eng.* 208 (2004) 189–208. <https://doi.org/10.1002/nme.1057>.

- [28] M.A. Bouaziz, J. Marae Djouda, F. Hild, On Mesoscale Strain Fluctuations in Tensile Tests on Additively Manufactured 17-4PH Stainless Steel, *J. Strain Anal. Eng. Des.* 57 (2022) 688–701.
- [29] M.D.C. Ferreira, W.S. Venturini, F. Hild, On the analysis of notched concrete beams: From measurement with digital image correlation to identification with boundary element method of a cohesive model, *Eng. Fract. Mech.* 78 (2011) 71–84.
<https://doi.org/10.1016/j.engfracmech.2010.10.008>.
- [30] R. Vargas, R.B. Canto, F. Hild, Journal of the European Ceramic Society Fracture energy evaluation of refractories in wedge splitting tests from notch opening displacements, *J. Eur. Ceram. Soc.* 41 (2021) 5367–5379.
<https://doi.org/10.1016/j.jeurceramsoc.2021.02.055>.
- [31] H. Leclerc, J. Neggers, F. Mathieu, F. Hild, S. Roux, Correli 3.0, IDD.N. FR. 001.520008. 000. SP 2015.000. 31500, 2015.
- [32] Z. Tomičević, F. Hild, S. Roux, Mechanics-aided digital image correlation, *J. Strain Anal. Eng. Des.* 48 (2013) 330–343. <https://doi.org/10.1177/0309324713482457>.